Observational features of charge distribution in Earth's inner magnetosphere

Check for updates

Lai Gao [1], Chao Shen [1] ✉, Yufei Zhou [1], Yong Ji[2], Zuyin Pu[3], George Parks[4], Christopher T. Russell [5], Gang Zeng [6], Lan Ma[1], Roy B. Torbert [7], Yanyan Yang[8,9] & James L. Burch [10]

Understanding the motion of charged particles in the electromagnetic field in the inner magnetosphere is essential for space science and space weather. Charge accumulation can occur due to the dipole magnetic and convective electric fields in this region. However, until the recent Magnetospheric Multiscale (MMS) mission, there were few means to detect charge distribution in situ. We report unambiguous in situ observation of the spatial distribution of the excess charge density in the inner magnetosphere by the MMS mission. We find that a positive (negative) charge accumulates in the dusk (dawn) side inner magnetospheres, which is contrary to the long assumed overall quasi-neutrality of space plasma. These observations and results offer insight into magnetosphere–ionosphere coupling.

The inner magnetosphere is a significant and intricate area of magnetospheric research. The dipole region of the magnetosphere close to Earth is called the inner magnetosphere[1]. It spans from approximately 1 to 10 Earth radii and includes a dipole magnetic field, a co-rotating electric field resulting from Earth's rotation, and a convection electric field generated by the solar wind[2]. These fields interact with the plasma present in space and give rise to three large-scale structures: the plasmasphere[3,4], the ring current[5–9], and the radiation belts[10,11], each corresponding to a population of particles having energies within a certain range. Low-energy particles that exit the ionosphere are influenced by the convection and co-rotating electric fields, which form the plasmasphere and can produce waves[12,13] that affect signal transmission between Earth and spacecraft[14]. Medium-energy particles are influenced by the magnetic field and travel around Earth, forming the ring current[15], which weakens the Earth's magnetic field[16,17]. High-energy particles in the radiation belts could 'kill' the instrument of spacecraft[18]. The inner magnetosphere plays a crucial role in the interactions between fields and plasma in space, energy conversion and matter transport, and serves as a key region in the research of the solar-magnetosphere–ionosphere coupling[19–22].

Medium- and high-energy particles that are consistently injected into the inner magnetosphere from the magnetotail are influenced by the convection electric field and dipole magnetic fields, resulting in two distinct types of paths within the inner magnetosphere[23]. One is open paths that extend from the magnetotail towards the dayside magnetopause, while the other is closed paths that orbit around the Earth. The boundary between the two types of paths is known as the Alfvén layer. To simulate the Alfvén layer, we adapted a previous analytic model for ring current particles[24], while assuming a dipole magnetic field with a uniform dawn-dusk electric field and a corotation electric field and setting the initial kinetic energies of protons and electrons to 6 keV and 2 keV, respectively, as shown in Fig. 1. We found that due to the opposite magnetic drift directions of electrons and ions, the Alfvén layer for electrons and ions is asymmetric and does not overlap completely, resulting in net charge accumulation near the separatrix path for particles of each sign. The phenomenon of charge accumulation in the inner magnetosphere was first proposed by Shield[25], but direct observational studies of the accumulation and distribution of charges have been limited due to experimental constraints.

The separation of charge generates a shielding electric field that protects the Earth's surface from harmful effects of the particles and radiation[26,27]. The charge discharge along magnetic field lines generate Region-2 field-aligned currents (FACs)[28] that flow into and out of the ionosphere on the dusk and dawn sides, respectively[29]. The Region-2 FACs

[1]School of Science, Harbin Institute of Technology, Shenzhen 518055, China. [2]School of Mathematics and Statistics, NingXia University, Yinchuan 750021, China. [3]School of Earth and Space Sciences, Peking University, Beijing, China. [4]University of California, Berkeley, CA 94720, USA. [5]Institute of Geophysics and Planetary Physics, University of California, Los Angeles, CA, USA. [6]School of Mathematics and Physics, Jingchu University of Technology, Jingmen, China. [7]Institute for the Study of Earth, Oceans, and Space, University of New Hampshire, Durham, NH, USA. [8]Institute of Crustal Dynamics, China Earthquake Administration, Beijing, China. [9]Key Laboratory of Crustal Dynamics, China Earthquake Administration, Beijing, China. [10]Space Science and Engineering Division, Southwest Research Institute, San Antonio, TX, USA. ✉e-mail: shenchao@hit.edu.cn
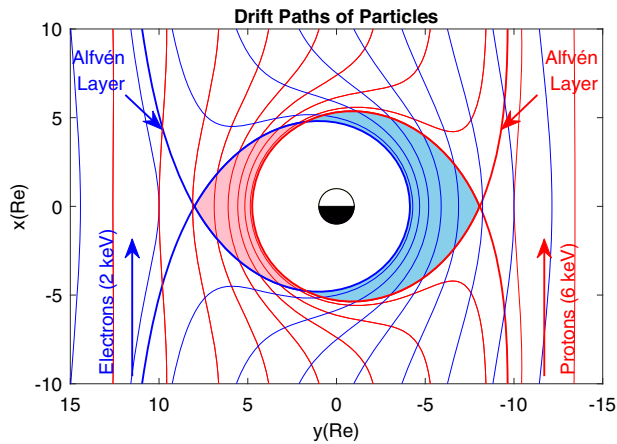
Fig. 1 | Illustration of the formation of the Alfvén layer viewed from the Northern Hemisphere with the sun at the top. The protons and electrons are injected into the inner magnetosphere from the plasma sheet on the night side under the action of a dawn–dusk electric field. The red and blue thin lines represent the drift paths of protons and electrons, respectively, in a dipole magnetic field with a uniform dawn–dusk electric field and a corotation electric field. The initial kinetic energies of protons and electrons are set to 6 keV and 2 keV, respectively. The red and blue thick lines denote the proton and electron Alfvén Layer, respectively. The pink area and sky-blue area indicate the regions where the positive and negative charges accumulate due to charge separation.

play an important role in space weather phenomena such as magnetic storms and substorms[30]. Understanding the charge distribution and the relationship between the electric field, charge, and geomagnetic activity is important in predicting and mitigating the impact of space weather.

The recent MMS mission[31], consisting of four identical spacecraft, has enabled highly accurate in situ four-point electric-field measurements and thus by Gauss's law the acquisition of space charge density, which has been further utilized to explore the electric properties of various space physics phenomena such as electron holes[32], magnetic reconnection[33], and magnetopause[34].

In this study, we utilized Gauss's law and the four-point electric field measurements made by MMS in Earth's inner magnetosphere to calculate the spatial distribution of the electric charge density there. We present two case studies at the dawn and dusk side respectively to show the features of charge density along the trajectories of the satellites. Furthermore, by using MMS data collected from 2015 through 2018, we perform a statistical investigation on the distribution of charge density in the inner magnetosphere and find that positive (negative) charges accumulate at dusk (dawn) and vary with geomagnetic conditions. The study reveals the presence of charge accumulation in the inner magnetosphere and confirms the existence of the Alfvén layer. The findings provide valuable insights into the plasma dynamics in the inner magnetosphere and can help clarify the magnetosphere-ionosphere energy exchange mechanism.

Results
Event analysis
On 17 December 2015, during a relatively quiet period with a maximum auroral electrojet index of 309 nT, we used data from the MMS mission as it moved from 8.8 Re away from Earth to 4 Re on the dusk side of the inner magnetosphere. As shown in Fig. 2b, the charge was always positive, the charge density (see the Methods section, calculation of charge density calculation) increased with decreasing L-shell, and the maximum charge density was 49 e m^{-3} at approximately $L = 5.91$. Additionally, the magnetic field intensity gradually increased from 65 nT to 487 nT, as shown in Fig. 2a. Figure 2e, f delineates spacecraft position at the start t_0 and end t_1 of the observation period.

Figure 3 shows the field and charge distributions on the dawn side on 23 February 2016 during a quiet period (maximum AE index was 174 nT). The

satellites moved from 4Re away from Earth to 10, as shown in Fig. 3e, f. As shown in Fig. 3a, the magnetic field intensity decreased gradually from 428 nT to 43 nT. As shown in Fig. 3b, the charge was always negative, and within $L = 7$, the charge density decreased sharply with increasing L-shell; the maximum negative charge density was -21 e m^{-3} at $L = 4$, and between $L = 7$ and $L = 9.8$, the charge density remained at approximately -3.47 e m^{-3}. As shown in Fig. 3c, d, the electric field displayed a high-frequency disturbance, and the overall trend was that the electric field intensity decreased with increasing L-value of the drift shell, similar to Fig. 2c, d.

The above comparison between the two cases reveals that positive (negative) charges accumulate at dusk (dawn), and the density decreases with increasing L-shell. To verify this case study and investigate the mechanism of charge accumulation, a statistical study of the net charge distribution is necessary.

Observations of electric field and electric charge density
We project E_y, $E_{||}$, and the charge density directly onto the equatorial plane in the solar magnetic (SM) coordinates along the magnetic field lines, assuming that the electric field is constant along a magnetic field line. To carry out a statistical study, first, we separate the data into three groups according to geomagnetic conditions as described by the AE index: (i) quiet times for AE<200nT, (ii) weakly disturbed periods for 200nT ≤ AE<500nT, and (iii) strongly disturbed periods for AE ≥ 500nT. Then, we separate the space according to L-shell and magnetic local time (MLT) with steps of $\Delta L = 0.5$ within $4 \leq L \leq 10$ and $\Delta MLT = 1h$ in the entire MLT region. Thus, in total, there are 12×24 bins in space. Finally, we calculate the average values for the electric field components E_y and $E_{||}$, as well as the electric charge density in each bin. During the quiet periods, the number of paths in each bin varied in the range of 4–69, whereas during the weakly and strongly disturbed periods, the corresponding ranges were much lower (1–32 and 0–16, respectively). The ratio of path numbers for the quiet, weakly disturbed, and strongly disturbed periods occupied 47.40%, 34.79%, and 17.79% of the whole observational duration, respectively.

Figure 4 shows the calculated results for the electric field (E_y, $E_{||}$) and the charge density after being projected and binned onto the equatorial plane in SM coordinates.

Figure 4a–c shows the distribution of E_y, where red corresponds to a duskward electric field ($E_y > 0$) and blue corresponds to a dawnward electric field ($E_y < 0$). During the quiet periods (i.e., in the early morning sector of 0–4 MLT with $L = 6$–10 and in the local time sector of 10–22 MLT on the dusk side with $L = 5$–10) are dawnward electric fields that contain the polarization field produced by the accumulated polarization charges in the Alfvén layer[25,26]. In the 5–8 MLT sector and the region limited by 22–24-4 MLT and $L = 4$–6 are duskward electric fields that are enhanced in disturbed periods and spread to cover 5–24 MLT, whereas the early morning sector of 0–6 MLT is dominated by a dawnward electric field. During strongly disturbed periods, E_y is enhanced overall.

Figure 4d–f shows the polarization charge distribution, where red corresponds to positive charges and blue corresponds to negative charges. Some positive charges gathered in 6–22 MLT in a limited L-shell range of $4 < L < 10$, and their density increased statistically with increasing geomagnetic disturbance. An azimuthally confined region of 0–6 MLT in quiet periods was occupied mainly by negative charges whose density was much smaller than that of the positive charges on the dusk side. During disturbed periods, the negative charges in this region seemed to fade away. The charge distributions on the dawn and dusk sides were generally consistent with the theoretical charge separation resulting from the grad-B drift and curvature drift of charged particles[35].

Next, we analyze the parallel electric field (Fig. 4g–i) that is closely related to the FACs. Because field-aligned electric fields are generated near the equatorial plane and are symmetrical with respect to it[36], the parallel components of the electric fields measured on the MMS away from the equator (>5°) in the magnetosphere can be divided into two categories: equatorward (blue) and poleward (red), with the poleward representing the direction from the equator to the South and North poles.

Fig. 2 | Overview of Observations by MMS on 17 December 2015. Overview of field and charge from the MMS constellation on 17 December 2015. **a** magnetic field intensity **B** at the center of the constellation, which is the average of the magnetic fields measured by the four spacecraft of MMS; **b** charge density ρ distribution; **c** electric field **E** at the center of the constellation, which is the average of the electric fields measured by the four spacecraft of MMS; **d** parallel electric field $E_{//}$; **e, f** the spacecraft positions.
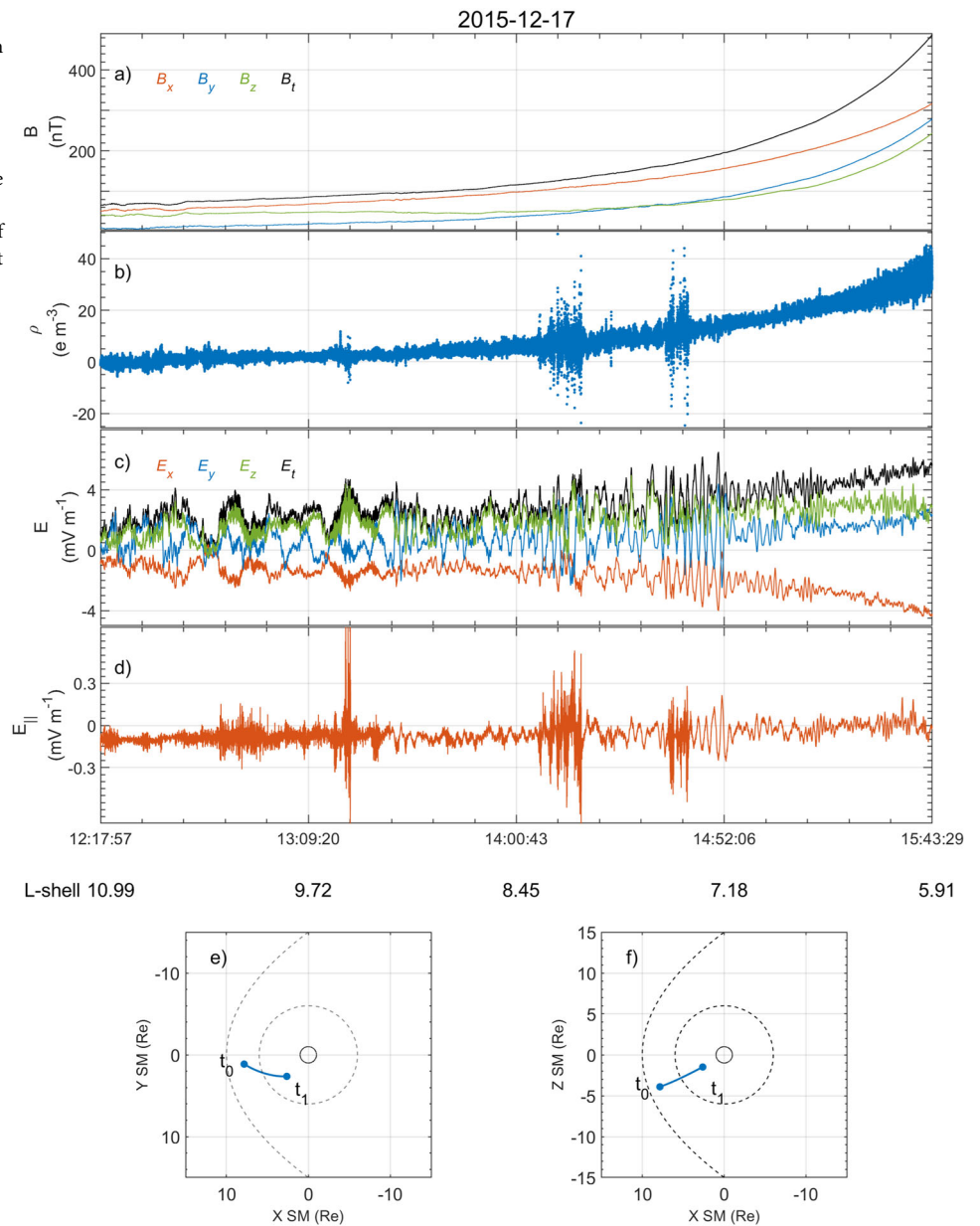
Figure 4d–i clearly shows a distributional accordance in the local time sector of 10–19 MLT between positive charges and the poleward parallel electric field and in 0–6 MLT between negative charges and the equatorward parallel electric field. This accordance can be explained by a direct application of Gauss's law that electric fields point away from positive charges (thus poleward for 10–19 MLT) and point toward negative charges (thus equatorward for 0–6 MLT). However, at 6–10 MLT at dayside, the accordance was contravened, perhaps because of some unknown physical processes in this local time sector require more-detailed studies in event analyses.

Two distinguished regions

The observations presented above reveal that there were two distinguished MLT sectors: (i) the local time sector limited by 13–16 MLT (sector A), where positive charges were accumulated, and (ii) the sector limited by 2–5 MLT (sector B), where negative charges were accumulated. The observations in these two sectors are consistent with the theoretical predictions for the dusk- and dawn-side parts of the Alfvén layer[25,36]. Then, we perform further analysis on the two sectors by averaging the charge density over

every $\Delta L = 0.1\text{Re}$ (horizontal axis) in Fig. 5a–c (sector A) and Fig. 5d–f (sector B) during different geomagnetic conditions (shown by the columns in the figures).

As shown in Fig. 5a, the charge density in sector A was positive. During quiet periods, the charge density diminished gradually towards the outer shells; for instance, it was 36.65 e m^{-3} at $L = 4$ and 15.39 e m^{-3} at $L = 10$; the same trend occurred during disturbed periods, as shown in Fig. 5b, c. By comparing Fig. 5a–c, it was evident that the positive charge accumulations grew with the geomagnetic disturbances. The maximum charge density for all L-shells was 47.97 e m^{-3} in weakly disturbed periods and 72.02 e m^{-3} in strongly disturbed periods.

As shown in Fig. 5d, the charge density in sector B during quiet periods was always negative, with an average value of -8.59 e m^{-3}; during disturbed periods, as shown in Fig. 5e, f, its magnitude diminished slightly.

By comparing the charge density distributions in Fig. 5a–f, in sector B on the dawn side, the amount of charge was significantly less than that in sector A on the dusk side. For $L = 4$–10, the average charge density in sector A was 22.92 e m^{-3} during quiet periods (approximately three times that in sector B) and 27.17 e m^{-3} during strongly disturbed periods [six times that in

Fig. 3 | Overview of Observations by MMS on 23 February, 2016. Overview of field and charge from MMS on 23 February 2016. **a** magnetic field intensity **B** at the center of the constellation, which is the average of the magnetic fields measured by the four spacecraft of MMS; **b** charge density ρ distribution; **c** electric field **E** at the center of the constellation, which is the average of the electric fields measured by the four spacecraft of MMS; **d** parallel electric field $E_{//}$; **e, f** the spacecraft positions.
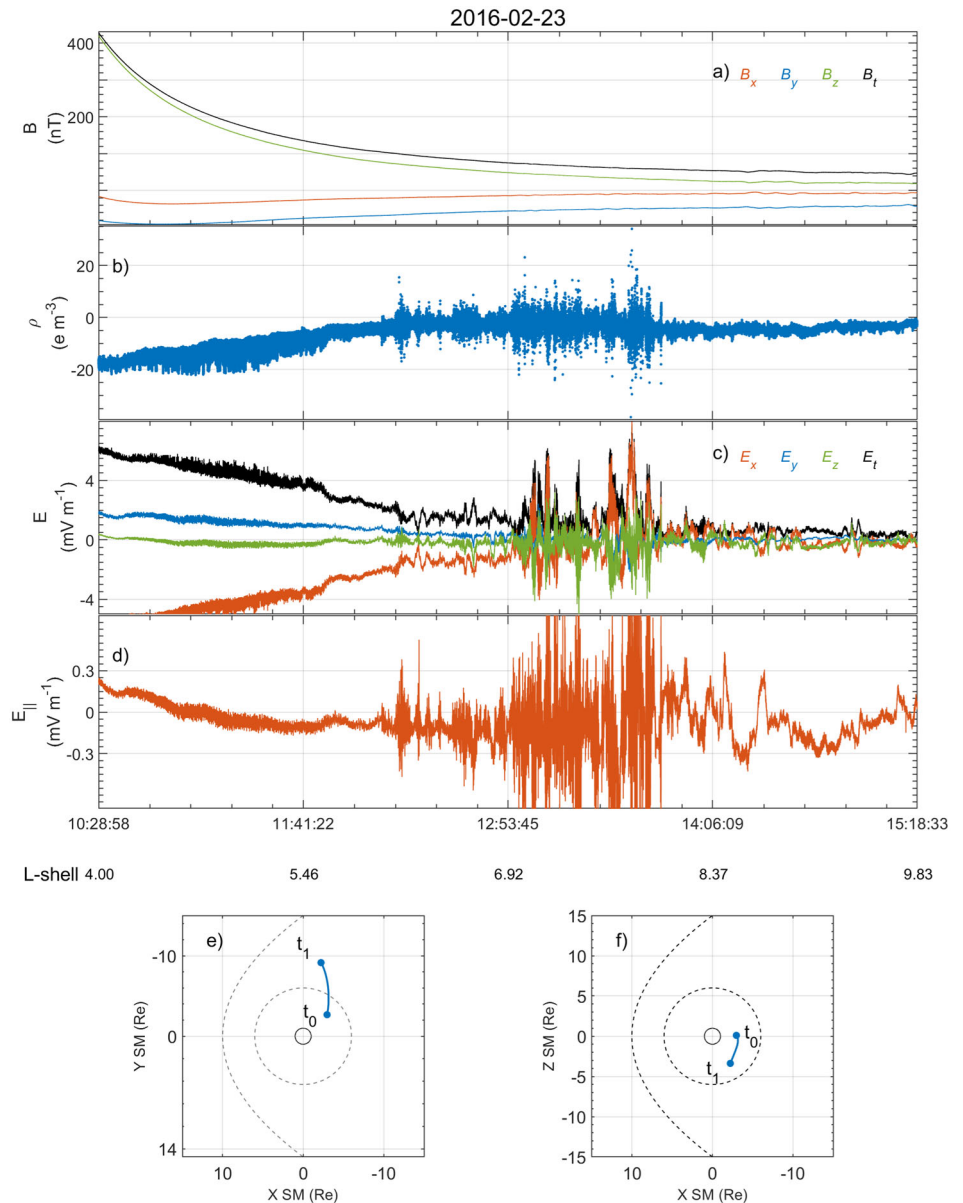
sector B (-4.93 e m^{-3})]. This finding implied a significant dawn–dusk asymmetry in the net charge distribution of the Alfvén layer in the inner magnetosphere, and this asymmetry become more severe with enhanced geomagnetic disturbances.

Conclusion

Based on the electric field data from the EDP onboard the MMS satellites, we revealed and analyzed the changes in the charge and electric field in the Earth's inner magnetosphere under different distribution conditions and exhibited, for the first time, the observational features of the Alfvén layer. The findings are summarized as follows. 1) The inner magnetosphere accumulates a positive charge at dusk and a negative charge at dawn. The charge decreases with increasing L-shell value and varies with magnetic activity. 2) The distributions of charge and electric field confirm the existence of charge separation in the Alfvén layer observed by multipoint satellites. 3) The charge distribution in the Alfvén layer has a dawn–dusk asymmetry, with the positive charge density at dusk being much greater than the negative charge density at dawn.

The data used in this study were measured during a solar minimum, and a few samples were collected for events with an AE index greater than

1000 nT. Future work is needed to study the charge distribution during periods of stronger geomagnetic activity.

Discussion

Here, we will explore additional intriguing phenomena that were not previously discussed. For instance, in examining Figs. 4 and 5, we observe a dawn-dusk asymmetry in charge density, contributing to the potential mechanism behind the asymmetry of the Alfvén layer. The current carriers for the Region-2 FACs should be protons and electrons. Given the substantial mass and inertia of protons, a robust field-aligned electric field on the twilight side is necessary to propel them into the ionosphere along magnetic field lines. Conversely, electrons, with their lesser mass and inertia, flow more readily into the ionosphere along magnetic field lines, even in the presence of a relatively weak field-aligned electric field. Figure 6 demonstrates how the Alfvén layers are connected to the polar ionosphere. The ionosphere discharges the Alfvén layers through geomagnetic field lines, creating the Region-2 FACs. The Poynting fluxes point toward the polar regions, facilitating the transfer of electromagnetic energy to the ionosphere. The discharge mechanism of charges into the ionosphere via Region-2 FACs remains uncertain due to the rarity of satellite magnetosynchronization in
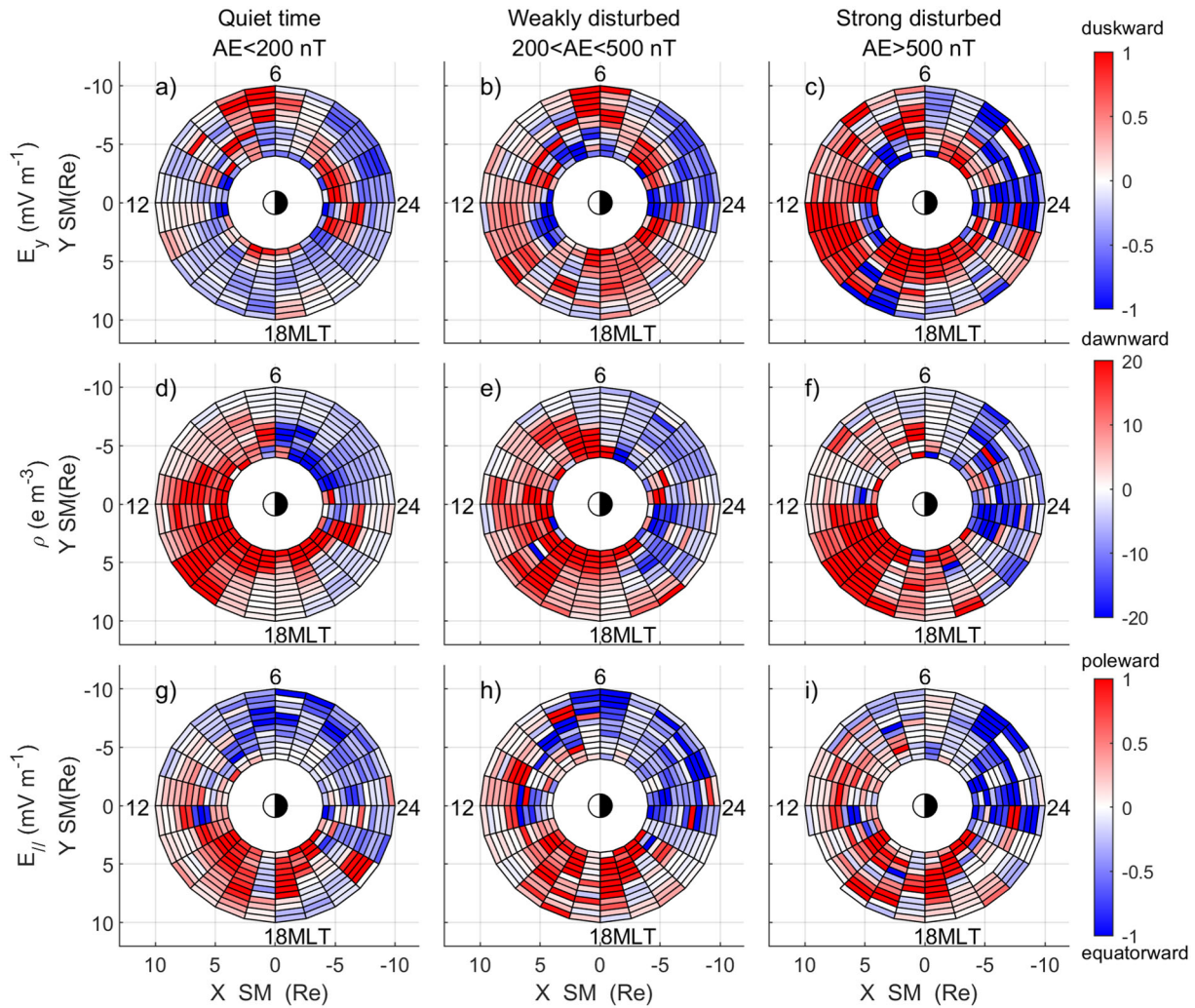
Fig. 4 | Statistical Results of Electric Fields and Charges. Spatial distributions of electric field and charge density derived from MMS data over all MLT(magnetic local time) and $4 \le L \le 10$ in the inner magnetosphere during three geomagnetic conditions (distinguished by the columns): **a–c** The y-component of the electric field E_y, **d–f** charge density ρ shown by their color scales, and (**g–i**) parallel electric field $E_{||}$ shown by its color scale, where red corresponds to a poleward electric field and blue to an equatorward field.

these regions and the underdeveloped technology for detecting charge densities in the ionosphere. Nevertheless, some evidence supports the significant role of Region-2 FACs in connecting the ionosphere and magnetosphere[37–39]. Notably, the comparison of FAC densities in the ionosphere and magnetosphere using Swarm and Cluster multispacecraft revealed similar latitudinal profiles despite notable differences in FACs transit times[40]. Observations also indicate a nearly constant current between Arase and AMPERE, implying a connection between the magnetosphere and the ionosphere through FACs at low latitudes, as the ratio of current density along the magnetic lines of force to the total magnetic field remains constant[41]. Anticipating future events conducive to joint observations with the ionosphere, we aim to gain a comprehensive understanding of the interaction between Region-2 FACs and charge accumulation, contributing to a deeper comprehension of the coupling mechanisms between the magnetosphere and the ionosphere.

In the realm of magnetospheric physics, the observed charge density in this study appears to be exceptionally high. This may be attributed to a lack of precision in the projection method. Owing to the characteristics of the Earth's dipole magnetic field, magnetic field lines become denser in the vicinity of the Earth's polar regions. Given that magnetic field lines represent equipotential lines, the charge density increases as the satellite gets closer to the Earth's polar region as indicated by the Poisson equation

($\rho = -\varepsilon_0 \nabla^2 \varphi$). Consequently, the charge density increases as the L value decreases. When estimating charge density along magnetic field lines, it is essential to scale it based on the density of the magnetic field lines, and the scaling factor is contingent on the corresponding magnetic field line density within the unit volume. Furthermore, in the observations of FACs, it has been noted that the distribution of these currents in the magnetosphere is transiently discontinuous, exhibiting discrete structures. When a satellite observes within the same flux tube, the observed charge density increases significantly. We have also considered the impact of satellite-induced electric fields, corotation electric fields, and satellite motion vorticity on charge density. The results suggest that these effects are minimal, although it is conceivable that other physical processes may counteract some of the impacts of charge separation in the Alfvén layer.

Figure 4 also shows that the electric field distribution and charge distribution have a westward rotation of 45°. It is commonly assumed that the electric current distribution is symmetrical at approximately 0–12 MLT in the magnetosphere and ionosphere[41–43], and that the convection electric field in the ionosphere is perpendicular to the line of 0–12 MLT[44]. However, as shown in Fig. 4, the axis of symmetry of the $E_{||}$ distribution is roughly at 3–15 MLT, and the equatorial electric field in the magnetosphere is mainly a tailward electric field. The phenomenon of westward rotation was also found in previous studies[45,46].
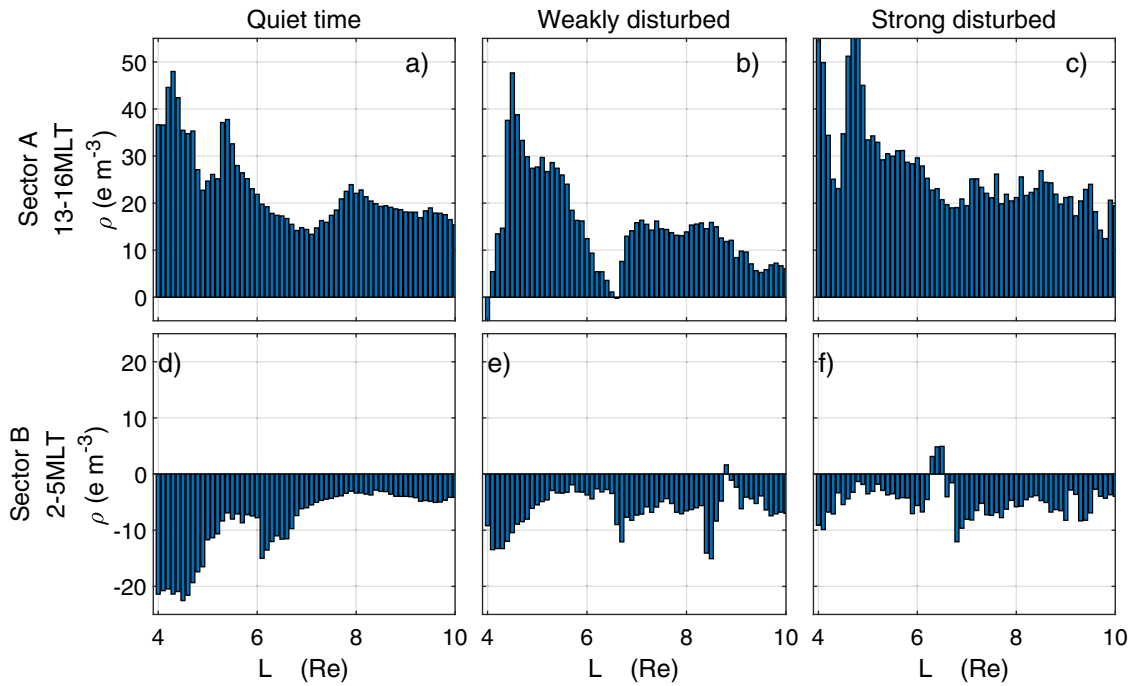
Fig. 5 | Comparative analysis of L-shell charge density distribution. a–c L-shell distribution of charge density in local time sectors 13–16 MLT (magnetic local time) (sector A) and (**d–f**): 2–5 MLT (sector B) during quiet, weakly disturbed, and strongly disturbed periods.

Fig. 6 | The plasmas convection in the inner magnetosphere creates the Alfvén layers, which act as dynamos to drive the Region-2 FACs J_{R2} connecting the polar ionosphere. The Poynting fluxes **S**, which are associated with the magnetic field disturbances δB generated by Region-2 FACs and the electric field **E** originated from the Alfvén layers, point toward the polar regions and transfer electromagnetic energy to the ionosphere.
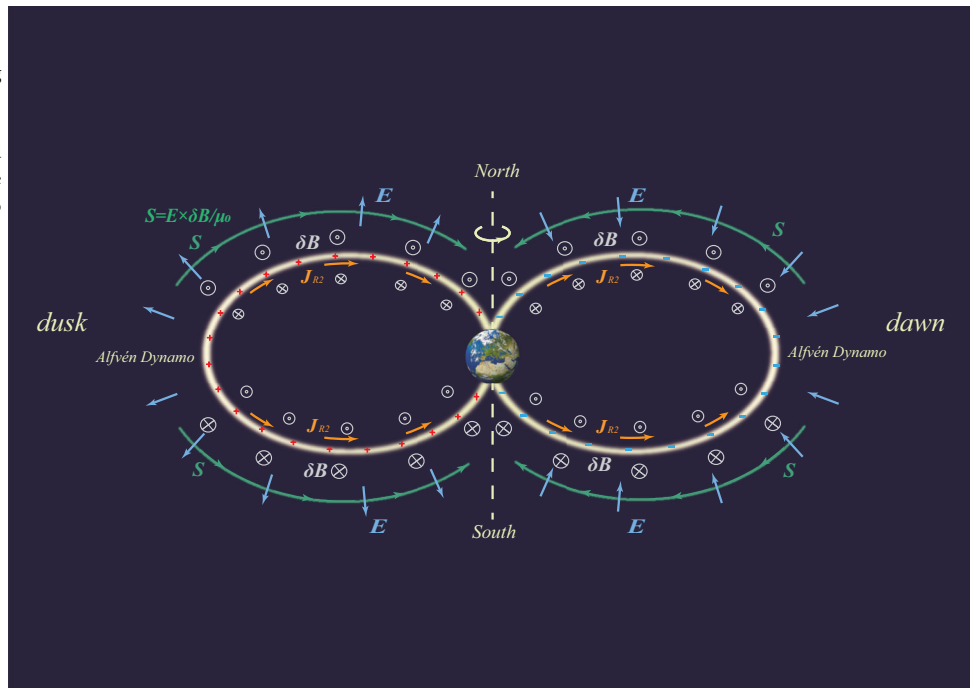
The region we observed, which is between 4–10 Re from Earth, partly overlaps with the plasmasphere that contains dense cold plasma with a density ranging from over $10^4 \mathrm{cm}^{-3}$ down to about 10 cm^{-3}, which is much greater than the charge density. Although charge compensation may occur, our statistical findings and individual event observations suggest that the charge compensation process in the plasmasphere cannot entirely offset the excess charge resulting from charge separation. It is unfortunate that the plasma data are severely missing when MMS is in the inner magnetosphere, despite being equipped with FPI instruments. Anticipated future advancements in measurement technologies hold the promise of providing more

nuanced data for a comprehensive understanding of the inner magnetosphere.

Methods
Charge density calculation
We use the electric- and magnetic-field data from all four MMS spacecraft that orbit Earth in near-equatorial space at low latitude with a perigee of 1.2 Re and an apogee of 12 Re. The data were collected three years from September 2015 to September 2018, during which the constellation swept the full range of MLT more than three times. The data from the field

instrument suite[47–49]—including electric field measurements—were provided by two sets of biased double-probe sensors (EDP)[50] with a temporal resolution of 8^{-1} s to 32^{-1} s.

For electric field data products, a quality indicator is provided, ranging from 0 to 3. In this scale, 0 denotes " very bad data or no data available," 1 denotes " bad data, use with caution," 2 denotes "fair data, use with caution," and 3 denotes " good data." In our research, we deliberately chose data products with quality indicators of 2 and 3, representing "ok" and "good" data, respectively. In the inner magnetosphere, the magnitude of the electric field is typically less than 100 mVm^{-1} [51,52], so to ensure statistical quality, we have removed any outliers whose values exceed 1000 mVm^{-1}.

Let the position vectors of the four MMS spacecraft be $\mathbf{r}_\alpha$ ($\alpha = 1, 2, \cdots, 4$) in barycentric coordinates[53], with $\frac{1}{4}\sum_{\alpha=1}^{4} \mathbf{r}_\alpha = 0$. The electric fields measured by the four spacecraft can be expressed as $\mathbf{E}_\alpha = \mathbf{E}(\mathbf{r}_\alpha)$, $\alpha = 1, 2, \cdots, 4$, and the linear gradient of component E_i of the electric field can be derived as follows[54]:

$$\nabla_j E_i = \frac{1}{4}\sum_{\alpha=1}^{4} E_{\alpha i} r_{\alpha k} R_{kj}^{-1} \quad (1)$$

where the volumetric tensor is defined as $R_{kj} = \frac{1}{4}\sum_{\alpha=1}^{4} r_{\alpha k} r_{\alpha j}$, which characterizes the constellation geometry. The truncation error for the gradient of the electric field is on the order of S/D, where S is the characteristic size of the constellation, and D is the spatial scale of the electric field[55]. The characteristic scale of MMS is generally $S \approx 20$ km, while the spatial scale of the electric field is assumed at the scale of one Earth radius (Re = 6371 km), as indicated by the empirical model of large-scale electric field in the inner magnetosphere[56]. So the truncation error for the gradient of the electric field is $(S/D)^2 \approx 0.0009\%$ [57], which implies the high accuracy of the calculation with formula (1). The four satellites are closely spaced so that the measured trends in the electric field are always consistent. This consistency suggests that the non-smoothness observed in the electric field represents a temporal oscillation, thus affirming the feasibility of using the spatial linear approximation[58] in charge calculations.

Based on the linear gradient of the electric field measured by each spacecraft, the charge density at the barycentre of the spacecraft constellation is calculated using Gauss's law as follows:

$$\rho = \varepsilon_0 \nabla \cdot E = \varepsilon_0 \sum_{i=1}^{3} \nabla_i E_i \quad (2)$$

To simulate the actual charge density measurement, we randomly placed a tetrahedron inside a non-uniformly charged sphere. The error in the charge calculation, denoted as $\Delta\rho/\rho = (\rho' - \rho)/\rho$, is defined as the difference between the charge density(ρ) calculated from the electric field divergence and the actual charge density ρ'. After running the model 1000 times with random tetrahedron shape inputs, we obtained a maximum error of 7.73% and an average error of 0.1%. These results suggest that the method used for the charge density calculation is reliable.

As shown previously, the observational error in the charge density calculated from MMS electric measurements is $\delta\rho \approx \varepsilon_0(\frac{\delta E_A}{S} + 2\frac{\delta E_S}{S})$, where the measurement accuracy of the axial electric field $\delta E_A < 1$mV/m, and the spin axial electric field $\delta E_S < 0.5$mVm^{-1}. So that $\delta\rho \approx 5.53$em^{-3}, where e is the charge of electron, and $e = 1.602\,176\,634 \times 10^{-19}$ Coulombs. Here, we remove outliers in the charge density (which accounted for less than 0.001% of all the data) whose values exceed 1000 e m^{-3}. Notably, the MMS constellation, at which the electric field is measured, is moving at an orbital velocity of approximately 1 ~ 10 km s^{-1} relative to Earth. The charge density calculated with Eq. (2) needs to be transformed under a Lorentz transformation[59] to obtain the corresponding charge density as viewed in the Earth center frame of reference. However, because the orbital speed of MMS is much less than the speed of light in a vacuum, the change in the charge density under the Lorentz transformation is small and well below the observational error of the charge density ($\delta\rho$) given above. Therefore, we neglect the effect of relativity here and assume that the charge density of the plasmas observed in the Earth center frame of reference is the same as that measured in the MMS constellation frame of reference.

Data availability

The datasets analyzed during the current study are publicly available from the MMS Science Data Center (https://lasp.colorado.edu/mms/sdc/public/), including magnetic fields from the Fluxgate Magnetometers (FGM) and the Electric field Double Probe (EDP). The geomagnetic activity data can be obtained from the OMNI data, provided by the Space Physics Data Facility at the NASA Goddard Space Flight Center (https://cdaweb.gsfc.nasa.gov/index.html).

Code availability

The Matlab code used for charge density calculation in this study can be obtained at https://github.com/LaiGao93/Charge-Density-Calculations.

References

1. Yiğit, E. Earth's Atmosphere and Geospace Environment. In *Atmospheric and Space Sciences: Neutral Atmospheres*, Vol. 1, (ed. Yiğit, E.) 41–51 (Cham: Springer International Publishing, 2015).
2. Usanova, M. E. & Shprits, Y. Y. Inner magnetosphere coupling: Recent advances. *J. Geophys. Res. Space Phys.* **122**, 102–104 (2017).
3. Carpenter, D. L. Whistler evidence of a 'knee' in the magnetospheric ionization density profile. *J. Geophys. Res.* **68**, 1675–1682 (1963).
4. Matsui, H. et al. Electric Fields and Magnetic Fields in the Plasmasphere: A Perspective From CLUSTER and IMAGE. *Space Sci. Rev.* **145**, 107–135 (2009).
5. Fok, M.-C. et al. New Developments in the Comprehensive Inner Magnetosphere-Ionosphere (CIMI) Model. *J. Geophys. Res. Space Phys.*, 126, https://doi.org/10.1029/2020JA028987 (2021).
6. Shen, C. et al. Direct calculation of the ring current distribution and magnetic structure seen by Cluster during geomagnetic storms. *J. Geophys. Res. Space Phys.* **119**, 2458–2465 (2014).
7. Williams, D. J. The Earth's ring current: Causes, generation, and decay. *Space Sci. Rev.* **34**, 223–234 (1983).
8. Le, G., Russell, C. T. & Takahashi, K. Morphology of the ring current derived from magnetic field observations. *Ann. Geophys.* **22**, 1267–1295 (2004).
9. Yang, Y. Y. et al. Storm time current distribution in the inner equatorial magnetosphere: THEMIS observations. *J. Geophys. Res. Space Phys.* **121**, 5250–5259 (2016).
10. Koskinen, H. E. J., & Kilpua, E. K. J. (2022). Radiation Belts and Their Environment. In *Physics of Earth's Radiation Belts: Theory and Observations* (eds. Koskinen, H. E. J. & Kilpua, E. K. J.) 1–25 (Cham: Springer International Publishing, 2022).
11. Lugaz, N. et al. Earth's magnetosphere and outer radiation belt under sub-Alfvénic solar wind. *Nat. Commun.* **7**, 13001 (2016).
12. Gallagher, D. L. et al. The Breathing Plasmasphere: Erosion and Refilling. *J. Geophys. Res. Space Phys.* **126**, e2020JA028727 (2021).
13. He, F. et al. Plasmapause surface wave oscillates the magnetosphere and diffuse aurora. *Nat. Commun.* **11**, 1668 (2020).
14. Denton, R. E. et al. Field line distribution of mass density at geostationary orbit. *J. Geophys. Res. Space Phys.* **120**, 4409–4422 (2015).
15. Kozyra, J. U. & Liemohn, M. W. Ring Current Energy Input and Decay. *Space Sci. Rev.* **109**, 105–131 (2003).
16. Consolini, G., De Michelis, P., & Tozzi, R. On the Earth's magnetospheric dynamics: Nonequilibrium evolution and the fluctuation theorem. *J. Geophys. Res. Space Phys.*, **113**, https://doi.org/10.1029/2008JA013074 (2008).
17. Shen, C., Zeng, G., Li, X. & Rong, Z. J. Evolution of the storm magnetic field disturbance around Earth's surface and the associated ring

current as deduced from multiple ground observatories. *J. Geophys. Res. Space Phys.* **120**, 564–580 (2015).

18. Lanzerotti, L. J. & Baker, D. N. Space weather research: Earth's radiation belts. *Space Weather* **15**, 742–745 (2017).

19. Fok, M.-C. Cross-regional coupling in *Ring Current Investigations* (eds Jordanova, Vania K. Ilie, R. & Chen, Margaret W.) 225–244 (Elsevier, 2020).

20. Fu, H. S. et al. IMAGE and DMSP observations of a density trough inside the plasmasphere. *J. Geophys. Res. Space Phys.* **115**, https://doi.org/10.1029/2009JA015104 (2010).

21. Fu, H. S. et al. The nightside-to-dayside evolution of the inner magnetosphere: Imager for Magnetopause-to-Aurora Global Exploration Radio Plasma Imager observations. *J. Geophys. Res. Space Phys.* **115**, https://doi.org/10.1029/2009JA014668 (2010).

22. Welling, D. T. et al. The Earth: Plasma Sources, Losses, and Transport Processes. *Space Sci. Rev.* **192**, 145–208 (2015).

23. Alfvén, H. On the Theory of Magnetic Storms and Aurorae. *Tellus* **10**, 104–116 (1958).

24. Shen, C. & Liu, Z. X. Properties of the neutral energetic atoms emitted from Earth's ring current region. *Phys. Plasmas* **9**, 3984–3994 (2002).

25. Schield, M. A., Freeman, J. W. & Dessler, A. J. A source for field-aligned currents at auroral latitudes. *J. Geophys. Res.* **74**, 247–256 (1969).

26. Wolf, R. A., Spiro, R. W., Sazykin, S. & Toffoletto, F. R. How the Earth's inner magnetosphere works: An evolving picture. *J. Atmos. Sol. Terrestrial Phys.* **69**, 288–302 (2007).

27. Wei, Y. et al. Long-lasting goodshielding at the equatorial ionosphere. *J. Geophys. Res. Space Phys.*, **115**, https://doi.org/10.1029/2010JA015786 (2010).

28. Kivelson, M., & Russell, C. *Introduction to Space Physics* (Cambridge: Cambridge University Press, 1995).

29. Iijima, T. & Potemra, T. A. Large-scale characteristics of field-aligned currents associated with substorms. *J. Geophys. Res. Space Phys.* **83**, 599–615 (1978).

30. Nakamizo, A. et al. Effect of R2-FAC development on the ionospheric electric field pattern deduced by a global ionospheric potential solver. *J. Geophys. Res. Space Phys.*, **117**, https://doi.org/10.1029/2012JA017669 (2012).

31. Burch, J., Moore, T., Torbert, R., & Giles, B. Magnetospheric Multiscale Overview and Science Objectives. *Space Sci. Rev.*, **199**, https://doi.org/10.1007/s11214-015-0164-9 (2015).

32. Tong, Y. et al. Simultaneous Multispacecraft Probing of Electron Phase Space Holes. *Geophys. Res. Lett.* **45**, 11,513–511,519 (2018).

33. Argall, M. R. et al. How neutral is quasi-neutral: Charge Density in the Reconnection Diffusion Region Observed by MMS. ESS Open Archive eprints 105, essoar.10501410, https://doi.org/10.1002/essoar.10501410.1 (2019).

34. Shen, C. et al. Measurements of the Net Charge Density of Space Plasmas. *J. Geophys. Res. Space Phys.* **126**, e2021JA029511 (2021).

35. Kavanagh, L. D. Jr, Freeman, J. W. Jr & Chen, A. J. Plasma flow in the magnetosphere. *J. Geophys. Res.* **73**, 5511–5519 (1968).

36. Ganushkina, N. Y., Liemohn, M. W. & Dubyagin, S. Current Systems in the Earth's Magnetosphere. *Rev. Geophys.* **56**, 309–332 (2018).

37. Dubyagin, S. et al. Storm time duskside equatorial current and its closure path. *J. Geophys. Res. Space Phys.* **118**, 5616–5625 (2013).

38. Robinson, R. M., Vondrak, R. R. & Potemra, T. A. Electrodynamic properties of the evening sector ionosphere within the region 2 field-aligned current sheet. *J. Geophys. Res. Space Phys.* **87**, 731–741 (1982).

39. Zhang, C. et al. Near Earth Vortices Driving of Field Aligned Currents Based on Magnetosphere Multiscale and Swarm Observations. *Chin. J. Space Sci.* **39**, 9 (2019).

40. Dunlop, M. W. et al. Simultaneous field-aligned currents at Swarm and Cluster satellites. *Geophys. Res. Lett.* **42**, 3683–3691 (2015).

41. Imajo, S. et al. Magnetosphere-Ionosphere Connection of Storm-Time Region-2 Field-Aligned Current and Ring Current: Arase and AMPERE Observations. *J. Geophys. Res. Space Phys.* **123**, 9545–9559 (2018).

42. Anderson, B. J., Korth, H., Waters, C. L., Green, D. L. & Stauning, P. Statistical Birkeland current distributions from magnetic field observations by the Iridium constellation. *Ann. Geophys.* **26**, 671–687 (2008).

43. Kunduri, B. S. R. et al. A Deep Learning-Based Approach for Modeling the Dynamics of AMPERE Birkeland Currents. *J. Geophys. Res. Space Phys.* **125**, e2020JA027908 (2020).

44. Huang, C.-S., Rich, F. J. & Burke, W. J. Storm time electric fields in the equatorial ionosphere observed near the dusk meridian. *J. Geophys. Res. Space Phys.* 115, https://doi.org/10.1029/2009JA015150 (2010).

45. Kikuchi, T. et al. Penetration of the convection and overshielding electric fields to the equatorial ionosphere during a quasiperiodic DP 2 geomagnetic fluctuation event. *J. Geophys. Res. Space Phys.*, **115**, https://doi.org/10.1029/2008JA013948 (2010).

46. Lui, A. T. Y. Inner magnetospheric plasma pressure distribution and its local time asymmetry. *Geophys. Res. Lett.*, **30**, https://doi.org/10.1029/2003GL017596 (2003).

47. Ergun, R. E. et al. The Axial Double Probe and Fields Signal Processing for the MMS Mission. *Space Sci. Rev.* **199**, 167–188 (2016).

48. Lindqvist, P. A., Olsson, G., Torbert, R. B. et al. The Spin-Plane Double Probe Electric Field Instrument for MMS. Space Sci Rev 199, 137–165. https://doi.org/10.1007/s11214-014-0116-9 (2016).

49. Russell, C. T. et al. The Magnetospheric Multiscale Magnetometers. *Space Sci. Rev.* **199**, 189–256 (2016).

50. Torbert, R. B. et al. The FIELDS Instrument Suite on MMS: Scientific Objectives, Measurements, and Data Products. *Space Sci. Rev.* **199**, 105–135 (2016).

51. Nishimura, Y., Shinbori, A., Ono, T., Iizima, M. & Kumamoto, A. Storm-time electric field distribution in the inner magnetosphere. *Geophys. Res. Lett.* **33**, https://doi.org/10.1029/2006GL027510 (2006).

52. Shinbori, A., Nishimura, Y., Ono, T., Kumamoto, A. & Oya, H. Electrodynamics in the duskside inner magnetosphere and plasmasphere during a super magnetic storm on March 13–15, 1989. *Earth Planets Space* **57**, 643–659 (2005).

53. Paschmann, G., & Daly, P. W. *Analysis Methods for Multi-Spacecraft Data*. ISSI Scientific Reports Series SR-001, ESA/ISSI, Vol. 1. (ISSI, 1998).

54. Shen, C. et al. Analyses on the geometrical structure of magnetic field in the current sheet based on cluster measurements. *J. Geophys. Res. Space Phys.*, **108**, https://doi.org/10.1029/2002JA009612 (2003).

55. Liu, Y. Y. et al. Failures of Minimum Variance Analysis in Diagnosing Planar Structures in Space. *Astrophys. J. Suppl. Seri.*, **267**, https://doi.org/10.3847/1538-4365/acdd58 (2023).

56. Matsui, H., Torbert, R. B., Spence, H. E., Khotyaintsev, Y. V. & Lindqvist, P. A. Revision of empirical electric field modeling in the inner magnetosphere using Cluster data. *J. Geophys. Res. Space Phys.* **118**, 4119–4134 (2013).

57. Shen, C. & Dunlop, M. Field Gradient Analysis Based on a Geometrical Approach. *J. Geophys. Res. Space Phys.* **128**, e2023JA031313 (2023).

58. Liu, Y. Y. et al. Testing the Linearity of Vector Fields in Cold and Dense Space Plasmas. *Astrophys. J.* **929**, 155 (2022).

59. Parks, G. K. Electric Field and Current. In *Characterizing Space Plasmas: A Data Driven Approach* (ed. G. K. Parks) 235–296 (Cham: Springer International Publishing, 2018).

Acknowledgements

nasa.gov/index.html) for making the geomagnetic activity data available through the OMNI dataset.

Competing interests
The authors declare no competing interests.

Additional information
Correspondence and requests for materials should be addressed to Chao Shen.

Peer review information *Communications Physics* thanks Huishan Fu, Joseph Borovsky and the other, anonymous, reviewer(s) for their contribution to the peer review of this work.

Reprints and permissions information is available at http://www.nature.com/reprints

Publisher's note Springer Nature remains neutral with regard to jurisdictional claims in published maps and institutional affiliations.